

MIT Open Access Articles

Modeling integrated photovoltaic-electrochemical devices using steady-state equivalent circuits

The MIT Faculty has made this article openly available. **Please share** how this access benefits you. Your story matters.

Citation: Winkler, M. T., C. R. Cox, D. G. Nocera, and T. Buonassisi. "Modeling integrated photovoltaic-electrochemical devices using steady-state equivalent circuits." Proceedings of the National Academy of Sciences 110, no. 12 (March 19, 2013): E1076-E1082.

As Published: <http://dx.doi.org/10.1073/pnas.1301532110>

Publisher: National Academy of Sciences (U.S.)

Persistent URL: <http://hdl.handle.net/1721.1/81303>

Version: Final published version: final published article, as it appeared in a journal, conference proceedings, or other formally published context

Terms of Use: Article is made available in accordance with the publisher's policy and may be subject to US copyright law. Please refer to the publisher's site for terms of use.



Modeling integrated photovoltaic–electrochemical devices using steady-state equivalent circuits

Mark T. Winkler^{a,1,2}, Casandra R. Cox^b, Daniel G. Nocera^{b,2}, and Tonio Buonassisi^{a,2}

Departments of ^aMechanical Engineering and ^bChemistry, Massachusetts Institute of Technology, Cambridge, MA 02139

Contributed by Daniel G. Nocera, January 25, 2013 (sent for review December 1, 2012)

We describe a framework for efficiently coupling the power output of a series-connected string of single-band-gap solar cells to an electrochemical process that produces storable fuels. We identify the fundamental efficiency limitations that arise from using solar cells with a single band gap, an arrangement that describes the use of currently economic solar cell technologies such as Si or CdTe. Steady-state equivalent circuit analysis permits modeling of practical systems. For the water-splitting reaction, modeling defines parameters that enable a solar-to-fuels efficiency exceeding 18% using laboratory GaAs cells and 16% using all earth-abundant components, including commercial Si solar cells and Co- or Ni-based oxygen evolving catalysts. Circuit analysis also provides a predictive tool: given the performance of the separate photovoltaic and electrochemical systems, the behavior of the coupled photovoltaic–electrochemical system can be anticipated. This predictive utility is demonstrated in the case of water oxidation at the surface of a Si solar cell, using a Co–borate catalyst.

Powering electrochemical reactions with photovoltaic devices to produce fuels provides an appealing solution to the societal need for clean energy (1). Although the deployment of photovoltaic modules has expanded rapidly over the last decade as costs have dropped (2), utilization of solar power is constrained by its local intermittency, thus providing an imperative for storage by the direct conversion of solar energy to chemical fuels. Photosynthetic organisms directly convert solar energy into chemical fuels by splitting water to produce molecular oxygen and hydrogen equivalents, which are fixed by their combination with carbon dioxide to produce carbohydrates. The technological imitation of photosynthesis—an “artificial leaf”—can be realized by integrating oxygen and hydrogen evolution catalysts to a semiconductor in a buried junction configuration (3). Most buried junction devices have relied on expensive solar cell architectures and/or catalysts (4), including those demonstrating solar-to-fuel efficiencies (SFEs) exceeding 18% (5–7). More economical artificial leaves have been realized with earth-abundant catalysts and solar cell materials but at reduced SFE (8, 9). We now seek to provide an analytical framework for the construction of higher SFE architectures comprising earth-abundant materials.

The efficiency of converting solar energy to stored chemical fuel has been considered (10–13) for a variety of configurations, including the specific treatment of buried junction devices (10). A primary result of these analyses is that single-junction solar cells are limited in powering water splitting with high SFE because solar cell materials that are well matched to the solar spectrum do not produce sufficient voltages to drive water splitting. Multijunction devices overcome this limitation, enabling high SFE by integrating several materials into a single multijunction device (5–7, 12). Despite their higher limiting SFEs, however, multijunction devices are costly; thus single-junction devices with higher SFEs would be preferred.

To this end, we explore in this contribution strategies to maximize the SFEs of designs, using a single absorber material. Whereas a single absorber is often unable to generate sufficient voltage to drive water splitting, arranging solar cells in series can increase

voltage and produce higher SFE. We describe the efficiency limitations faced by series-connected devices, emphasizing the fundamental efficiency-limiting role played by electrical coupling between the electrochemical and photovoltaic processes. In addition, we introduce a framework for modeling practical photovoltaic–electrochemical (PV-EC) devices and use it to analyze the design requirements for water splitting using series-connected Si solar cells. We focus on Si due to its lower cost and overwhelming market advantage (2). We develop the steady-state equivalent circuit (i.e., neglecting reactive elements) of a coupled PV-EC system and use it to demonstrate two important design capabilities. First, equivalent-circuit analysis enables modeling of realistic PV-EC systems. Consequently, it describes the impact of key parameters such as the Tafel slope of the catalysts, the diode ideality of the PV device, and the series and solution resistance of the PV and EC systems, respectively. Second, the performance of the coupled PV-EC system can be predicted via separate characterization of the PV device and the EC cell. We illustrate this capability using a practical PV-EC device (Si integrated with recently discovered Co-OEC (14–16) and Ni-OEC (17, 18) catalysts). We show that practical PV-EC devices using commercial Si solar cells and earth-abundant catalysts should be capable of yielding SFEs comparable to those of multijunction solar cells.

Results and Discussion

Device Construct. Fig. 1A illustrates a PV-EC using a PV, an electrochemical system, and a coupling system. The coupling system matches the electrical output (current and voltage) of the PV device to the electrical input of the EC process. In this arrangement, the steady-state efficiency η_{SF} with which solar power is transferred to chemical fuels is given by

Significance

This article extends the construction of direct solar-to-fuels devices, such as the artificial leaf based on crystalline silicon. Because a single Si junction has insufficient potential to drive water splitting, it cannot be used for direct solar-to-fuels conversion. This paper performs an equivalent circuit analysis for multiple series-connected devices. The predictive utility of the model is demonstrated in the case of water oxidation at the surface of a Si solar cell, using a cobalt–borate oxygen evolving catalyst. Considering recent cost reductions of Si solar cells, this paper offers a path to the construction of low cost solar-to-fuels devices.

Author contributions: M.T.W., C.R.C., D.G.N., and T.B. designed research; M.T.W. and C.R.C. performed research; M.T.W., C.R.C., and T.B. analyzed data; and M.T.W., D.G.N., and T.B. wrote the paper.

The authors declare no conflict of interest.

Freely available online through the PNAS open access option.

¹Present address: Physical Sciences Division, IBM T. J. Watson Research Center, Yorktown Heights, NY 10598.

²To whom correspondence may be addressed. E-mail: nocera@mit.edu, mwinkler@post.harvard.edu, or buonassisi@mit.edu.

This article contains supporting information online at www.pnas.org/lookup/suppl/doi:10.1073/pnas.1301532110/-DCSupplemental.

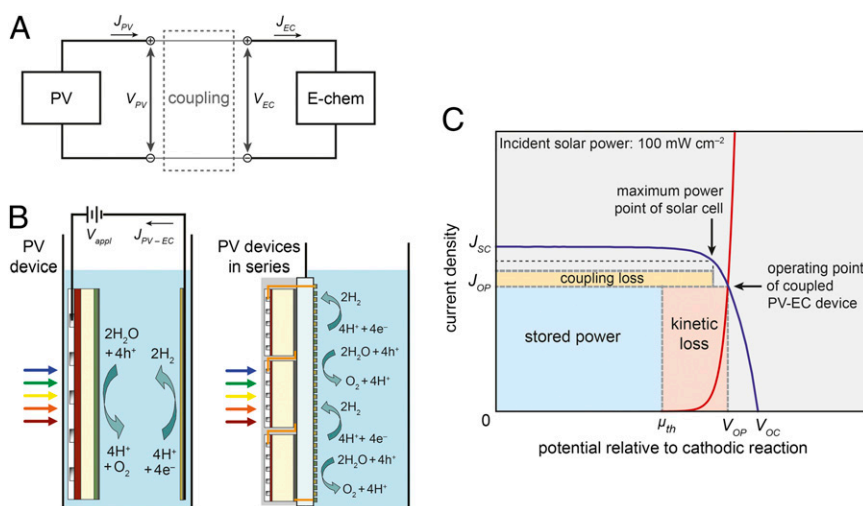


Fig. 1. (A and B) (A) Block diagram for providing power to an electrochemical cell (EC), using a photovoltaic (PV) device via direct coupling, as well as (B) experimental examples, including an interdigitated contact geometry that minimizes solution resistance. (C) The generalized current density-voltage (J - V) diagram of a directly coupled PV-EC device graphically identifies the power flows relative to total incident solar power. The plot represents a maximally efficient solar cell ($\eta_{pv} = 30.8\%$) with open circuit voltage V_{oc} and short-circuit current density J_{sc} ; total plot area is scaled to incident solar power (100 mW·cm⁻²). The PV-EC system operates at the intersection of the current-voltage curves. At the operating current density J_{op} , power $J_{op}V_{op}$ is dissipated whereas energy is stored at a rate of $J_{op}\mu_{th}$ (where μ_{th} is the thermodynamic reaction potential). The difference represents overpotential losses. Coupling loss is defined as the difference between the solar cell maximum output and the power dissipated in the electrochemistry. These losses are represented in region $J > J_{op}$.

$$\eta_{SF} = \eta_{pv} \times \eta_{ec} \times \eta_c, \quad [1]$$

where η_{pv} , η_{ec} , and η_c are the efficiencies of the PV device, the EC process, and the coupling arrangement, respectively (19).

The efficiency η_{pv} of a solar cell is thermodynamically limited. The maximum efficiency varies as a function of the absorber's band gap E_g and exhibits a broad efficiency maximum of about 30% (20) near $E_g \sim 1.2$ eV. Although this is near the water-splitting potential, a solar cell's maximum voltage is thermodynamically limited to be 300–400 mV lower than E_g/q at room temperature (21). Technologically, these thermodynamic limits are approached only by mature materials such as Si and GaAs (22). The maximum voltage and current of a cell are measured under open- and short-circuit conditions and are referred to as V_{oc} and J_{sc} , respectively. The maximum power output of a solar cell occurs at a current J_{mp} and voltage V_{mp} smaller than these maximum values and is often expressed as $FF \times J_{sc}V_{oc}$, with the fill factor, $FF = J_{mp}V_{mp}/J_{sc}V_{oc}$. The fill factor is thermodynamically limited to be in the range 0.8–0.9 for most materials of interest (21), but imperfections such as series resistance (see Eq. 7 or Fig. 3A) yield lower values. Given the solar irradiance P_{sun} , the efficiency of a solar cell is thus

$$\eta_{pv} = \frac{FF \times V_{oc} \times J_{sc}}{P_{sun}}. \quad [2]$$

When N identical solar cells are connected in series, their output voltages sum while the current density decreases as $1/N$. (If cells are arranged next to each other in a plane perpendicular to the incident light, total current is constant but area grows as N . Alternatively, the cells can be arranged along the direction of incident light propagation as in ref. 8. In this case, the area presented to incident light remains constant, each cell absorbs only a fraction of the incident light, and total current drops as $1/N$. In both cases, current density drops as $1/N$.) In practice, variations in cell-to-cell performance will reduce the overall efficiency of the series-connected cells; such “mismatch losses” are not explicitly considered in Eq. 2.

The efficiency η_{ec} of an electrochemical process is generally dominated by kinetic limitations rather than thermodynamic ones. The operating voltage V_{op} must exceed the thermodynamic potential μ_{th} to achieve a sufficient reaction rate or operating current density J_{op} . For a fuel-generating reaction, the power flow into the stored chemical energy is $\mu_{th}J_{op}$ whereas the total electrical energy dissipated is $V_{op}J_{op}$. Thus, the efficiency of the electrochemical reaction is

$$\eta_{ec} = \mu_{th}/V_{op}. \quad [3]$$

In the case of the water-splitting reaction, the oxygen evolution reaction (OER) occurs at the anode and the hydrogen evolution reaction (HER) occurs at the cathode. The HER can be catalyzed at low overpotentials relative to the OER; thus this efficiency is usually dominated by the choice of OER catalyst (23). At the current densities necessary for a PV-EC device, earth-abundant catalysts provide OER overpotentials that range from 0.25 to 0.4 V, corresponding to η_{ec} in the range of 75–85%. Lower overpotentials are possible with non-earth-abundant materials such as RuO₂ (4).

The efficiency η_c of the coupling system is entirely dependent on the choice of implementation, and its efficiency is not limited by any fundamental consideration. In principal, the simplest way to couple the systems may be to perform the anodic and cathodic reactions on the positive and negative terminals of a buried junction (or series of solar cells), respectively. In the case of water splitting, this geometry is sometimes referred to as an artificial leaf (3). We refer to this coupling scheme, or any other in which the two half-reactions occur on surfaces equipotential with the terminals of a solar cell, as direct electrical connection; it describes both wired and wireless water splitting (Fig. 1B). Fig. 1A illustrates that direct electrical connection is equivalent to constraining the currents and voltages of the PV device and the EC system to be identical: $J_{pv} = J_{ec}$ and $V_{pv} = V_{ec}$. Graphically, this constraint identifies the operational state of the coupled PV-EC device as the point at which the steady-state current-voltage properties of the PV device and the EC system intersect (24). This mode of operation may result in the solar cell producing less

than its maximum output ($V_{op}J_{op} < V_{mp}J_{mp}$). Referring to Eq. 2, the coupling efficiency is

$$\eta_c = \frac{V_{op} \times J_{op}}{FF \times V_{oc} \times J_{sc}}. \quad [4]$$

Alternatives to direct coupling are also possible. For example, power electronics could convert the electrical output of one or more solar cells to the required electrical input of the electrochemistry. Practically, the choice of a coupling scheme would be dictated by matching the tolerable complexity, reliability, and cost of an application with available coupling solutions.

Using the above expressions, Eq. 1 can be rewritten as

$$\eta_{SF} = \frac{FF \times V_{oc} \times J_{sc}}{P_{sun}} \times \frac{\mu_{th}}{V_{op}} \times \frac{V_{op} \times J_{op}}{FF \times V_{oc} \times J_{sc}} = \frac{\mu_{th} \times J_{op}}{P_{sun}}. \quad [5]$$

The final term of Eq. 5 represents the SFE of an electrochemical reaction driven by solar power. In Fig. 1C, we summarize each of these efficiency terms graphically. We note that, because the HER occurs on the negative terminal of the solar cell, the x axis of Fig. 1C is referenced to a reversible hydrogen electrode (RHE) and is thus invariant with pH.

We consider the scenario in which only a single type of PV absorber is used. Single-absorber technologies compose the vast majority of the terrestrial PV market (25), so it seems likely that deployment of PV-EC devices, at a scale meaningful relative to the energy economy, would require the lowest-cost, most widely available solar cell technology. Currently, Si and CdTe dominate this category, although technologies such as $\text{Cu}(\text{In}_{1-x}\text{Ga}_x)\text{Se}_2$ and GaAs are also in commercial production (25). For single-absorber solar cells to generate a voltage sufficient to drive a reaction, several cells may have to be wired in series. For example, an outstanding Si solar cell produces a maximum voltage of about 700 mV (22). Thus, at least two cells, wired in series, would be required to drive the water-splitting reaction ($\mu_{th} = 1.23$ V). If an excess of cells were added in series, however, the operating point of the coupled PV-EC system would fall far from the maximum power point of the cell (Fig. 2B: e.g., note the intersection of the $R_{sol} = 0$ electrochemical curve with the three- and four-cell curves).

Such analysis permits calculating the limiting efficiency for any electrochemical reaction powered by a single-absorber solar cell. First, the current density output J_{op} from a series arrangement of N ideal solar cells is calculated at the voltage equivalent

to the thermodynamic potential of a reaction μ_{th} . The SFE is then calculated using Eq. 5. The number of cells N is chosen to maximize the SFE. The results of this calculation are shown in Fig. 2A. Because Fig. 2A represents ideal solar cells and electrochemistry, it primarily reflects the impact of direct electrical coupling on the thermodynamics of solar energy conversion. The high-contrast lines in Fig. 2A identify conditions at which the addition or subtraction of a cell dramatically changes the efficiency the PV-EC system. A representative scenario is shown in Fig. 2B (which illustrates coupling for the practical devices considered in Fig. 3B) at the point marked by the red asterisk. Although ideal PV and EC systems are used to generate Fig. 2A, the implication that impedance matching is critical for efficient operation of PV-EC devices is generalizable to nonideal cases. Practical cases are considered in *PV-EC Equivalent Circuit and Device Modeling* and this calculation is replicated with practical inputs in Fig. S1.

The maximum theoretical SFE for series-connected single absorbers is 30.8% and occurs for a solar cell with $E_g = 1.38$ eV. Because the calculation treats electrochemistry as ideal ($\eta_{ec} = 1$), the optimal efficiency and band gap are identical to those for an ideal solar cell (21). Correspondingly, the only (ideal) electrochemical reactions that could be carried out at this efficiency would be those for which μ_{th} is equal to the voltage at the maximum power point of the solar cell device (s). To obtain $V_{mp} = \mu_{th}$ (and thus $\eta_c = 1$), the reaction must occur at $\mu_{th} = N \times 0.93$ V, where N is an integer. For water splitting ($\mu_{th} = 1.23$ V), the maximum SFE is 27.5% and it occurs for two series-connected cells with $E_g = 1.04$ eV; the efficiency when Si ($E_g = 1.12$ eV) powers the reaction is only slightly smaller ($\eta_{SF} = 26.9\%$). Critically, we note that most materials well matched to the solar spectrum ($1.0 \text{ eV} < E_g < 2.0 \text{ eV}$) exhibit theoretical efficiencies at or above 20% provided that an appropriate number of cells are placed in series; some relevant technologies are shown in Table 1.

PV-EC Equivalent Circuit and Device Modeling. Solar cells and electrochemical reactions do not operate at thermodynamic limits. The electrical behavior of practical PV and EC systems can be described in steady state, using equivalent circuits (Fig. 3A). Circuit analysis enables accurate modeling of PV-EC devices and provides insight into their realistic performance and efficiency limitations.

The equivalent circuit of a PV device is well known (26). In a PV device, light absorption generates a current of excited

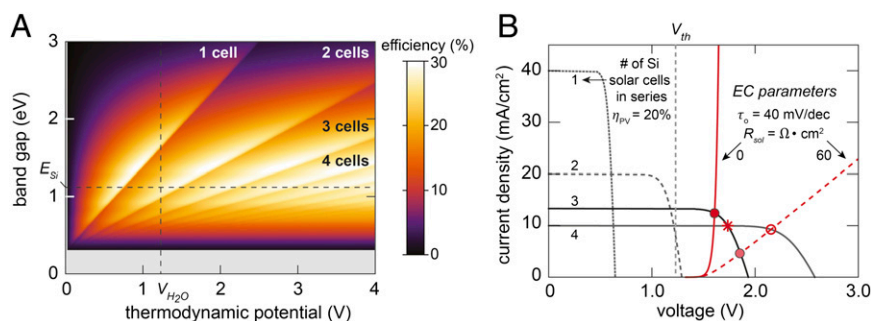


Fig. 2. (A) Density plot of the efficiency of using the output power of an ideal solar cell (band gap E_g) to produce and store chemical energy via reversible electrochemical (EC) reactions (thermodynamic reaction potentials μ_{th}). Considering only single-band-gap solar cells, EC reactions with μ_{th} larger than solar cell operating voltages require multiple cells in series. The plot exhibits regions defined by the number of cells required for efficient coupling, characterized by band gap E_g , to produce stored chemical energy via reversible EC reactions defined by thermodynamic reaction potentials μ_{th} . Because only single-band-gap solar cell materials are considered, EC reactions with μ_{th} larger than the operating voltages of the solar cells ($\sim E_g/q - 350$ mV, where q is the fundamental charge) require multiple cells in series. The plot is separated by areas of rapidly changing efficiency into regions defined by the number of solar cells required for efficient coupling. (B) Current density-voltage plot indicating the impact of electrochemical parameters on the coupling efficiency and the number of realistic Si solar cells ($\eta_{th} = 20\%$) required. Overlaid points correspond to solutions also shown in Fig. 3B.

Table 1. Theoretical limiting efficiency for common solar cell absorbers when powering ideal water splitting

Material	E_g/eV	$\eta_{\text{SF}} \times 100\%$
c-Si*	1.12	26.9
Cu(In _{1-x} Ga _x)Se ₂	1.15 [†]	26.1
GaAs	1.42	19.7
CdTe	1.44	19.2
a-Si [‡]	1.7	26.8

*Crystalline silicon.

[†]Band gap is representative of high-efficiency Cu(In_{1-x}Ga_x)Se₂ devices (32).

[‡]Amorphous silicon.

electrons and holes that relax by recombining, some by flowing through an external circuit with current density J_{PV} . Although a well-designed solar cell maximizes J_{PV} , some photogenerated carriers are lost to internal recombination via one or more recombination mechanisms. Each recombination current can generally be described by a diode equation,

$$J_n(V) = J_0 \left[\exp\left(\frac{V}{nV_{\text{th}}}\right) - 1 \right] \approx J_0 \exp\left(\frac{V}{nV_{\text{th}}}\right), \quad [6]$$

where J_0 is the saturation current density that describes the equilibrium rate of the mechanism and $V_{\text{th}} = k_b T/q$ is the thermal voltage (given by the electron charge q , temperature T , and Boltzmann constant k_b). The approximation on the right side of Eq. 6 is accurate at typical solar cell operating voltages. The value of the ideality factor n depends on the recombination mechanism, but the use of one or two recombination currents is often sufficient to provide an accurate description of most high-performance materials. Ohmic losses can be modeled by introducing a series resistance R_s that modifies the output device voltage, and shunt paths that bypass the intended circuit can be approximated by a resistance R_{sh} . The output current density J_{PV} is the difference between the generated photocurrent J_L and the recombination currents,

$$J_{\text{PV}}(V) = J_L - J_{0,1} \exp\left(\frac{V + J_{\text{PV}}R_s}{n_1 V_{\text{th}}}\right) - J_{0,2} \exp\left(\frac{V + J_{\text{PV}}R_s}{n_2 V_{\text{th}}}\right) - \frac{V + J_{\text{PV}}R_s}{R_{\text{sh}}}. \quad [7]$$

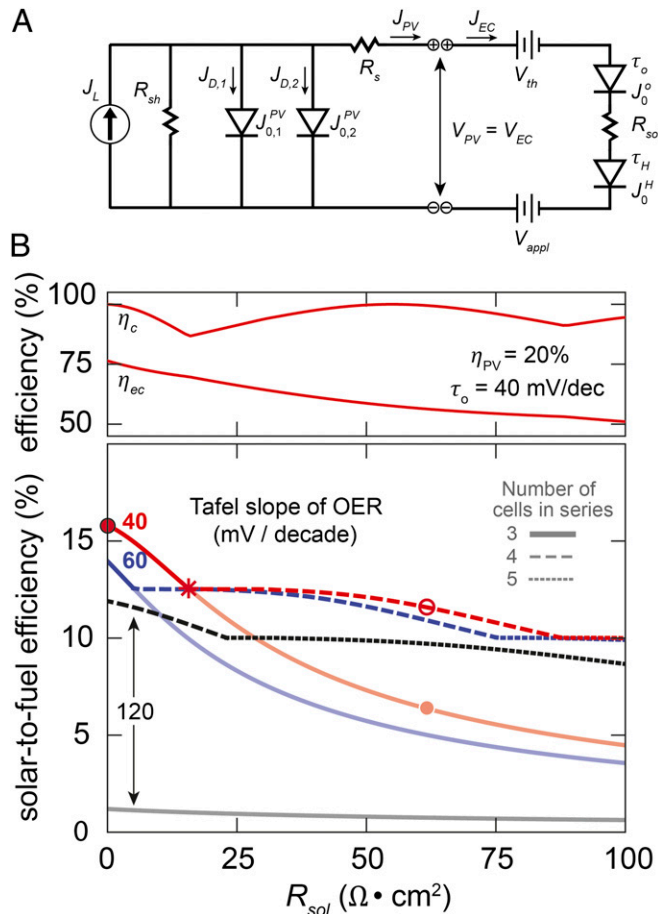


Fig. 3. (A) Steady-state equivalent circuit of a PV-EC system coupled via direct electrical connection. An applied voltage is incorporated for analysis of externally assisted reactions. **(B)** The efficiencies of Eq. 1 for electrochemical water splitting as a function of solution resistance for various values of OER Tafel slope. The power source is comparable to commercially available Si solar cells ($\eta_{\text{PV}} = 20\%$, Tables 2 and 3). Operation at overlaid points corresponds to matching points in Fig. 2B. Solar-to-fuel efficiency can exceed 15%; the contributing efficiencies of the electrochemistry (η_{ec}) and the system coupling (η_c) are specified for an OER Tafel slope of 40 mV/decade. Minima in η_c occur when the optimal number of solar cells changes.

Eq. 7 is represented using typical circuit components in Fig. 3A. If N identical solar cells are wired together in series, their voltages are additive whereas the current density of the entire system will decrease as $1/N$. This feature can be approximated by defining $J_{\text{PV}}^N(NV) = J_{\text{PV}}(V)/N$.

An electrochemical reaction proceeds only when the voltage between two electrodes exceeds the thermodynamic potential μ_{th} of the reaction by an amount sufficient to drive the reaction kinetics. The voltage V necessary to drive an electrochemical current density J_{ec} is given by adding the thermodynamic potential, the overpotential for each reaction (given by the Tafel law), and the Ohmic losses to solution resistance R_{sol} . For the water-splitting reaction, the OER and the HER are the electrochemical reactions of interest, and the necessary voltage is given by

$$V = \mu_{\text{th}} + \tau_{\text{O}} \log\left(\frac{J_{\text{ec}}}{J_0^{\text{O}}}\right) + \tau_{\text{H}} \log\left(\frac{J_{\text{ec}}}{J_0^{\text{H}}}\right) + J_{\text{ec}} R_{\text{sol}}. \quad [8]$$

In Eq. 8, the terms τ and J_0 are the Tafel slope and the exchange current density, respectively. The OER and the HER are each characterized by a distinct τ and J_0 , identified in Eq. 8 by the superscripts “O” and “H,” respectively. The impact of these kinetic parameters has been explored in detail (24). For the purpose of completing the circuit diagram of the steady-state behavior of the PV-EC device, we note that the Tafel law is mathematically identical to the diode equation. For example, the current-voltage properties of the OER are given by

$$V_{\text{OER}} - V_{\text{th}}^0 = \tau_{\text{O}} \log\left(\frac{J_{\text{ec}}}{J_0^{\text{O}}}\right), \quad [9]$$

where all parameters are as defined above, but in this case V_{th}^0 is the Nernstian potential for the OER. It is clear that Eq. 9 has the same form as the diode equation (Eq. 6) under the substitutions $V_{\text{OER}} - V_{\text{th}}^0 \rightarrow V$, $\tau_{\text{O}} \rightarrow nV_{\text{th}}$, and $J_0^{\text{O}} \rightarrow J_0$. Thus, each electrochemical reaction can be represented as a diode operating under a reverse bias equal to the thermodynamic or Nernstian potential; this condition is represented in Fig. 3A.

The circuit shown in Fig. 3A can be solved to model the coupled PV-EC system. Under the constraint that $J_{\text{ec}} = J_{\text{PV}}$, Eqs. 7 and 8 can be solved numerically for the operational

voltage, current density, and resulting SFE (given a set of device characteristics for the PV device and the EC system). For example, assuming that the system is powered by high-performance, commercially available silicon solar cells ($\eta_{\text{pv}} = 20\%$), the behavior of the system under different electrochemical parameters can be explored along with the number of solar cells required to optimally couple the system. Fig. 3B illustrates the impact of solution resistance and OER Tafel slope (see Tables 2 and 3 for the parameters). OER catalysts produce different Tafel slopes depending on their mechanism; in this work, Tafel slopes of 120, 60, and 40 mV/decade are considered. In each scenario, the operating voltage and resulting efficiency are found when power is provided by an optimal number of N identical solar cells wired in series.

To ensure optimal coupling, the value of N changes depending on the performance of the rest of the system; for the range of parameters studied, anywhere between three and five cells are required. The points at which N changes value are evident in Fig. 3B by kinks in the curve (for clarity, the efficiency for coupling to $N = 3$ is shown for all values of R_{sol}). Fig. 2B illustrates the graphical solution for several points on the curves in Fig. 3B (for $\tau_o = 40$ mV/decade and $R_{\text{sol}} = 0$ and $60 \Omega\cdot\text{cm}^2$); these points are denoted in both figures by solid and open circles. For $R_{\text{sol}} = 0$, it is clear that three series-connected solar cells provide a higher operating current (at a nearly identical operating voltage) than a four-cell arrangement. For $R_{\text{sol}} = 60 \Omega\cdot\text{cm}^2$, however, the overpotential increases significantly and requires four series-connected solar cells to achieve significant currents; Fig. 2B illustrates this fact at points marked by open red and solid red circles.

The SFE exceeds 15% provided a high-performance OER catalyst ($\tau_o = 40$ mV/decade) and low solution resistance ($R_{\text{sol}} < 10 \Omega\cdot\text{cm}^2$) are realized. SFE exceeds 10% for all but the least attractive electrochemical parameters studied ($\tau_o = 120$ mV/decade and $R_{\text{sol}} > 40 \Omega\cdot\text{cm}^2$), indicating that the low SFE observed for water splitting with earth-abundant materials stems from using low-efficiency solar cell devices (8, 27) and/or poor electrical coupling. Thus, a high-efficiency ($\eta_{\text{SF}} > 10\%$) PV-EC device should be feasible using entirely earth-abundant components operating at or near neutral pH. Appropriate catalysts have been demonstrated (14–18), and PV-device design can minimize R_{sol} . Given electrode spacing d and solution conductivity G , Ohmic losses are $\Delta V = J_{\text{op}} R_{\text{sol}} \sim J_{\text{op}} \times d/G$. Thus, electrode geometry can minimize Ohmic losses even in relatively low conductivity solutions. Fig. 1B (Right) illustrates a design in which solar cells are coupled to the electrolyte via interdigitated contacts; using standard screen printing, electrode spacing could be reduced to $d < 100 \mu\text{m}$. For $J_{\text{op}} \sim 15 \text{ mA}\cdot\text{cm}^{-2}$ and $G = 50 \text{ mS}\cdot\text{cm}^{-1}$ (achievable at neutral pH), Ohmic losses would be reduced to $\Delta V = 3$ mV. Treating this voltage drop as an increase in the overpotential, Eq. 3 indicates a negligible impact on SFE of $\sim 0.2\%$ relative. In this geometry, however, H_2 and O_2 are proximately evolved, and crossover is minimized owing to the selectivity of the catalyst design (i.e., the OER catalysts do not oxidize H_2 because H_2 does not coordinate to Co/Ni-Pi/Bi oxidic clusters and vice versa O_2 reduction by the HER catalysts is minimal). In this design, however, H_2 and O_2 must be separated. This issue has been considered in the case of anodes and cathodes on separate

Table 3. Solar cell parameters for the modeling results shown in Fig. 3B

J_0	$4 \times 10^{-10} \text{ mA}\cdot\text{cm}^{-2}$
R_s	$1.5 \Omega\cdot\text{cm}^2$
V_{oc}	669 mV
J_{sc}	$41 \text{ mA}\cdot\text{cm}^{-2}$

surfaces within an electrochemical cell (28, 29), but would need to be readdressed for an interdigitated, coplanar geometry.

Although it is clear from Fig. 3B that better catalysis and lower solution resistance are desirable for higher SFE, Fig. 3B also illustrates the trade-offs when directly coupling a PV and EC system. In some scenarios, the quality of catalysis governs the efficiency. For example, given inefficient catalysis (Tafel slope of 120 mV/decade), SFE exceeding 10% is possible only if the optimal number of solar cells is wired in series ($N = 4$) and R_{sol} is minimal. In this particular case, the coupling efficiency $\eta_c \sim 1$ and efficiency losses beyond those in the solar cell are governed by a high overpotential (~ 1 V), leading to $\eta_{\text{ec}} = 0.57$. Moreover, if only three solar cells are wired in series in this instance, the SFE is minimal due to extremely inefficient coupling: Even at $R_{\text{sol}} = 0$, the system efficiencies are ($\eta_{\text{pv}}, \eta_c, \eta_{\text{ec}}$) = (0.20, 0.09, 0.62). For 60- and 40-mV/decade catalysis, on the other hand, SFEs approaching or exceeding 15%, respectively, are possible. For a system with low R_{sol} , coupling is almost perfect (Fig. 2B, solid red circle), and losses beyond those of the PV device originate only from the small overpotential [for 40 mV/decade at $R_{\text{sol}} = 0$, ($\eta_{\text{pv}}, \eta_c, \eta_{\text{ec}}$) = (0.20, 1.00, 0.76)]. Fig. 3B emphasizes that achieving high SFE relies on many interdependent factors.

We distill from these analyses several design guidelines for PV devices used in a PV-EC system. First, increasing the current of a PV device will always produce a proportionate increase in SFE, whereas an increased voltage will not. This observation is evident from Eq. 5, and Fig. S2 clarifies this point graphically. One consequence of this observation is that higher-efficiency solar cells do not always provide a proportionate increase in the solar-to-fuels efficiency. For example, the most efficient Si solar cell in commercial production has an efficiency $\eta_{\text{pv}} = 23.6\%$ (30); however, it achieves this efficiency through higher voltages ($V_{\text{oc}} = 727$ mV) rather than higher currents ($J_{\text{sc}} = 40 \text{ mA}\cdot\text{cm}^{-2}$), relative to the 20% cell modeled above. As a result, η_{SF} increases only by about 6% relative (from 15.3 to 16.3%). This increase is due to moving the operating point closer to short-circuit conditions (emphasized in Fig. S2). Similarly, modeling the highest-efficiency single-junction solar cell ever produced [a GaAs solar cell with $\eta_{\text{pv}} = 28.8\%$ (22)] increases η_{SF} to an impressive 18.2%, but this SFE still underperforms the improvement in PV efficiency significantly. An underlying reason for this is that the cell voltage ($V_{\text{oc}} = 1.12$ V) couples less efficiently to the water-splitting reaction ($\eta_c = 0.83$). We elaborate on both of these examples in Figs. S1–S3.

The second design guideline is that the sensitivity of the PV-EC system to solution resistance is highly dependent on conditions of coupling: namely, if a system is not optimally coupled, it may be relatively insensitive to changes in solution resistance. This observation is clear in Figs. 2B and 3B and particularly evident in Fig. S3. The optimal coupling for OER I conditions

Table 2. Electrochemical parameters for the modeling results shown in Fig. 3B

	Tafel slope, mV/decade	Exchange current density, $\text{mA}\cdot\text{cm}^{-2}$
OER kinetics		
Case I	40	5×10^{-12}
Case II	60	100×10^{-12}
Case III	120	250×10^{-12}
HER kinetics	30	1×10^{-2}

(Table 2) occurs at $R_{\text{sol}} = 0$. At this point, the system is highly sensitive to increases in R_{sol} , which shift the system to higher operating voltages and a region of rapidly decreasing PV-device currents (higher voltages than the solid red circle in Fig. 2B). However, once the operating point shifts to the four-cell curve (at about $15 \Omega\text{-cm}^2$), R_{sol} has very little impact on SFE until it reaches $\sim 60 \Omega\text{-cm}^2$ (traversing from the * to the open red circle in Fig. 2B or Fig. 3B). In general, for a solar cell with voltage V_{mp} at the maximum power point, the SFE will be relatively invariant to increases in R_{sol} of approximately $\Delta R = V_{\text{mp}}/J_{\text{op}}$. The cell modeled here exhibits $V_{\text{mp}} = 528 \text{ mV}$ and $J_{\text{op}} \sim 10 \text{ mA}\cdot\text{cm}^{-2}$, yielding $\Delta R = 50 \Omega\text{-cm}^2$ and good agreement with the width of the SFE “plateaus” in Fig. 3B. This effect is more pronounced for cells with higher operating voltages, as is evident in Fig. S3.

Practical Implications. PV-EC systems such as the artificial leaf pose challenging integration issues beyond those related to the photovoltaic and electrochemical processes alone. In particular if the PV-EC design is wireless, and the entire PV device is immersed in the electrolyte, nontrivial materials challenges must be met to ensure device stability in the vicinity of highly oxidizing conditions (5, 27). Thus, predicting device performance without performing the integration saves substantial research effort.

Consideration of Fig. 1A, as well as the discussion of Figs. 1C and 2B, makes clear that such predictions are possible if the current-voltage properties of the isolated PV and EC systems are known. As discussed, a PV-EC system coupled via direct electrical connection operates under the constraint that $J_{\text{pv}} = J_{\text{ec}}$ and $V_{\text{pv}} = V_{\text{ec}}$, a condition that can be found graphically as the intersection of the current-voltage properties. Provided that these properties are known for the PV and EC systems, it is straightforward to identify this operational point.

As a case study, we analyze the OER half-reaction in an experiment nearly identical to that described previously (31). In this experiment, the positive terminal of a Si solar cell is functionalized with the CoB_i catalyst; the Si surface is protected by established methods (31). Because this reaction is powered by a single solar cell, the reaction must be assisted with an externally applied voltage, V_{appl} . This voltage is accommodated in Eq. 8 (or Fig. 3A) by substituting $V \rightarrow V + V_{\text{appl}}$, eliminating the term related to the HER, and replacing the thermodynamic potential with the Nernstian potential for the OER given the solution pH.

In Fig. 4 (Inset), we demonstrate graphically how the illuminated characteristics of this PV-EC system can be found at an applied voltage V_{appl} . The current-voltage curve of the OER (obtained via steady state Tafel analysis in isolation from the solar cell) is shifted to the lower potentials by the applied voltage; the resulting intersection predicts the behavior of the PV-assisted electrochemical reaction. In Fig. 4, the predicted behavior of the coupled PV-EC system is compared with experiment by using the J - V characteristics of the PV device (not shown for clarity) and the Tafel analysis of the cobalt-borate (CoB_i) catalyst (measured in the dark and isolated from the solar cell). The data and the prediction agree to within $<10 \text{ mV}$. This framework provides insight into interpreting PV-assisted EC reactions. For example, it has been noted that the onset of water oxidation may be reduced by a voltage approximately equal to the solar cell V_{oc} (31). Under the present analysis, we note that the Tafel analysis was performed at current densities at or below $1 \text{ mA}\cdot\text{cm}^{-2}$; inspection of Fig. 4 (Inset) reveals that at such a current density, the system must be coupled near the solar cell's open-circuit potential and thus a comparable voltage will be used for the electrochemical process.

Conclusion

We have outlined a framework for integrating single-absorber solar cells as power sources for electrochemical processes and understanding the efficiency-limiting elements. The steady-

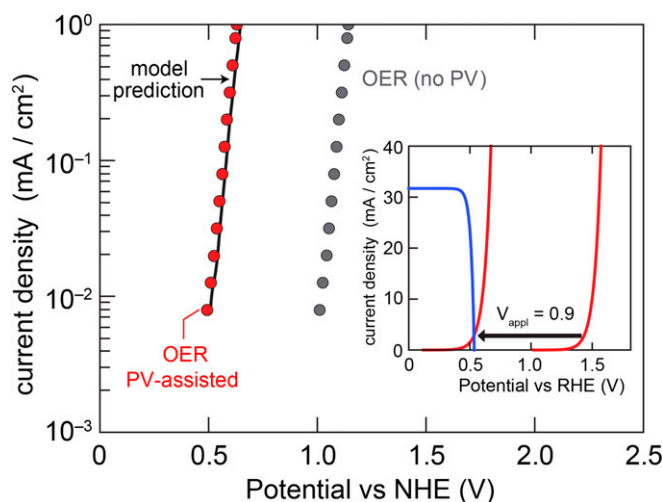


Fig. 4. Predicted Tafel behavior of a PV-EC system in PV-assisted water oxidation similar to that in ref. 31. The electrical properties of the PV and EC systems, measured independently, are used to predict the coupled behavior. (Inset) Graphical demonstration of the predictive analysis for PV-assisted reactions.

state efficiency of coupled PV-EC systems depends on the individual efficiency of each system, but it also depends critically on the efficiency of coupling the two systems. When coupling the two systems directly, by performing each half-reaction on a terminal of the PV device, the coupling efficiency can be modeled using a steady-state equivalent circuit. Additionally, the efficiency of the coupled PV-EC system can be determined given the behavior of each subsystem. We validate this model by correctly predicting the J - V characteristics of a PV-assisted OER to within $<10 \text{ mV}$. A key result of our analysis is that even when using commercially available Si solar cells, SFE over 15% is achievable provided the design yields very low solution resistance. We have proposed strategies for meeting this challenge.

Experimental Procedures

Sample fabrication and experimental procedures for collecting the data in Fig. 4 have been described in detail (31). We provide a summary and describe any differences here. Crystalline Si solar cells were improved relative to the procedures of ref. 31 by including a Si_3N_4 antireflection layer (75 nm thick, deposited by low-pressure chemical vapor deposition) atop the emitter surface and by optimizing the emitter contact pattern, using photolithography to reduce resistive losses and shadowing. These design changes improved J_{sc} from $27 \text{ mA}\cdot\text{cm}^{-2}$ to $34 \text{ mA}\cdot\text{cm}^{-2}$ and increased the FF from 0.47 to 0.77; consequently, the efficiency improved from 7 to 13%. A 100-nm Ni passivation layer (used in place of indium tin oxide because it functions comparably and facilitates soldering wires to the cell) was deposited by dc sputtering as part of an extensive exploration of catalysts and passivation layers (33). Following Ni deposition, the cobalt-borate (CoB_i) catalyst was deposited. Bulk electrolysis was performed in a two-compartment electrochemical cell with a glass frit junction of fine porosity. For the electrodeposition, the working compartment was charged with $\sim 50 \text{ mL}$ of solution (25 mL of 0.2 M KB_i electrolyte and 25 mL of 1 mM Co^{2+} solution). The auxiliary compartment was charged with $\sim 50 \text{ mL}$ of 0.1 M KB_i electrolyte. The working electrode was the Ni-coated surface of a $1.5 \times 2\text{-cm}^2$ piece of the Si solar cell. Typically, a 1-cm^2 area of the working electrode was immersed in the solution and electrolysis was carried out at 0.85 V vs. NHE until $26 \text{ mC}\cdot\text{cm}^{-2}$ of charge passed.

Photoelectrochemistry experiments were performed in a one-compartment quartz cell. The light source was a Sol 2A solar simulator (Newport). The Tafel behavior of surface-passivated, catalyst-functionalized solar cells was measured in the region of water oxidation over a 200-mV range in 10- to 30-mV increments. The measurements were conducted in a solution containing 0.5 M KB_i and 1.5 M KNO_3 at pH 9.2, using an Ag/AgCl reference electrode and a Pt auxiliary electrode.

ACKNOWLEDGMENTS. The authors acknowledge helpful conversation with Joep Pijpers, Christine Simmons, Joseph Sullivan, and Yogesh Surendranath. This work was supported through National Science Foundation (NSF) Faculty Early Career Development Program ECCS-1150878 (to T.B.), Air Force Office of Scientific Research Grant FA9550-09-1-0689 (to D.G.N.), the National Research Foundation Singapore through the Singapore MIT

Alliance for Research and Technology's Low Energy Electronic Systems research program (T.B.), and a generous gift from the Chesonis Family Foundation. This work was performed in part at Harvard University's Center for Nanoscale Systems, a member of the National Nanotechnology Infrastructure Network, which is supported by the NSF under Award ECS-0335765.

1. Cook TR, et al. (2010) Solar energy supply and storage for the legacy and nonlegacy worlds. *Chem Rev* 110(11):6474–6502.
2. Powell DM, et al. (2012) Crystalline silicon photovoltaics: A cost analysis framework for determining technology pathways to reach baseload electricity costs. *Energy Environ Sci* 5:5874–5883.
3. Nocera DG (2012) The artificial leaf. *Acc Chem Res* 45(5):767–776.
4. Yamane S, et al. (2009) Efficient solar water splitting with a composite “n-Si/p-CuI/n-i-p a-Si/n-p GaP/RuO₂” semiconductor electrode. *J Phys Chem C* 113:14575–14581.
5. Khaselev O, Turner JA (1998) A monolithic photovoltaic-photoelectrochemical device for hydrogen production via water splitting. *Science* 280(5362):425–427.
6. Khaselev O, Bansal A, Turner JA (2001) High-efficiency integrated multijunction photovoltaic/electrolysis systems for hydrogen production. *Int J Hydrogen Energy* 26(2):127–132.
7. Peharz G, Dimroth F, Wittstadt U (2007) Solar hydrogen production by water splitting with a conversion efficiency of 18%. *Int J Hydrogen Energy* 32:3248–3252.
8. Rocheleau RE, Miller EL, Misra A (1998) High-efficiency photoelectrochemical hydrogen production using multijunction amorphous silicon photoelectrodes. *Energy Fuels* 12(1):3–10.
9. Kelly NA, Gibson TL (2006) Design and characterization of a robust photoelectrochemical device to generate hydrogen using solar water splitting. *Int J Hydrogen Energy* 31:1658–1673.
10. Rocheleau RE, Miller EL (1997) Photoelectrochemical production of hydrogen: Engineering loss analysis. *Int J Hydrogen Energy* 22:771–782.
11. Weber MF, Dignam MJ (1986) Splitting water with semiconducting photoelectrodes—efficiency considerations. *Int J Hydrogen Energy* 11:225–232.
12. Bolton J, Strickler S, Connolly J (1985) Limiting and realizable efficiencies of solar photolysis of water. *Nature* 316:495–500.
13. Ross RT, Hsiao TL (1977) Limits on the yield of photochemical solar energy conversion. *J Appl Phys* 48:4783–4785.
14. Kanan MW, Nocera DG (2008) In situ formation of an oxygen-evolving catalyst in neutral water containing phosphate and Co²⁺. *Science* 321(5892):1072–1075.
15. Surendranath Y, Kanan MW, Nocera DG (2010) Mechanistic studies of the oxygen evolution reaction by a cobalt-phosphate catalyst at neutral pH. *J Am Chem Soc* 132(46):16501–16509.
16. Surendranath Y, Lutterman DA, Liu Y, Nocera DG (2012) Nucleation, growth, and repair of a cobalt-based oxygen evolving catalyst. *J Am Chem Soc* 134(14):6326–6336.
17. Dincă M, Surendranath Y, Nocera DG (2010) Nickel-borate oxygen-evolving catalyst that functions under benign conditions. *Proc Natl Acad Sci USA* 107(23):10337–10341.
18. Bediako DK, et al. (2012) Structure-activity correlations in a nickel-borate oxygen evolution catalyst. *J Am Chem Soc* 134(15):6801–6809.
19. Kelly NA, Gibson TL, Cai M, Spearot JA, Ouwkerk DB (2010) Development of a renewable hydrogen economy: Optimization of existing technologies. *Int J Hydrogen Energy* 35:892–899.
20. Shockley W, Queisser H (1961) Detailed balance limit of efficiency of p-n junction solar cells. *J Appl Phys* 32:510–519.
21. Henry C (1980) Limiting efficiencies of ideal single and multiple energy-gap terrestrial solar-cells. *J Appl Phys* 51:4494–4500.
22. Green MA, Emery K, Hishikawa Y, Warta W, Dunlop ED (2013) Solar cell efficiency tables (v. 41). *Prog Photovolt Res Appl* 21:1–11.
23. Surendranath Y, Nocera DG (2011) Oxygen evolution reaction chemistry of oxide-based electrodes. *Prog Inorg Chem* 57:505–560.
24. Surendranath Y, Bediako DK, Nocera DG (2012) Interplay of oxygen-evolution kinetics and photovoltaic power curves on the construction of artificial leaves. *Proc Natl Acad Sci USA* 109(39):15617–15621.
25. Mehta S (2012) 28th annual cell & module data collection results. *Greentech Media* 31:1–24.
26. Green MA (2003) Crystalline and thin-film silicon solar cells: State of the art and future potential. *Sol Energy* 74(3):181–192.
27. Reece SY, et al. (2011) Wireless solar water splitting using silicon-based semiconductors and earth-abundant catalysts. *Science* 334(6056):645–648.
28. Haussener S, et al. (2012) Modeling, simulation, and design criteria for photoelectrochemical water-splitting systems. *Energy Environ Sci* 5:9922–9935.
29. Hernández-Pagán EA, et al. (2012) Resistance and polarization losses in aqueous buffer-membrane electrolytes for water-splitting photoelectrochemical cells. *Energy Environ Sci* 5:7582–7589.
30. Smith DD, et al. (2012) Generation III high efficiency lower cost technology. *Proceedings of the 38th IEEE Photovoltaics Special Conference* (IEEE, Piscataway NJ), pp 001594–001597.
31. Pijpers JJH, Winkler MT, Surendranath Y, Buonassisi T, Nocera DG (2011) Light-induced water oxidation at silicon electrodes functionalized with a cobalt oxygen-evolving catalyst. *Proc Natl Acad Sci USA* 108(25):10056–10061.
32. Contreras MA, et al. (2005) Diode characteristics in state-of-the-art ZnO/CdS/Cu(In_{1-x}Ga_x)Se₂ solar cells. *Prog Photovolt Res Appl* 13:209–216.
33. Cox CR, Winkler MT, Pijpers JJH, Buonassisi T, Nocera DG (2013) Interfaces between water splitting catalysts and buried silicon junctions. *Energy Environ Sci* 6(2):532–538.